Automated Segmentation of Adipose Tissue in Magnetic Resonance Images of the Whole Body

Christian Wuerslin, *Student-Member, IEEE,* Bin Yang, *Member, IEEE,* Juergen Machann, and Fritz Schick

***Abstract*—The amount and the bodily distribution of different adipose tissue (AT) compartments are important indicators for the risk of obesity-related diseases and play an important role in the investigation of their pathogenesis. Magnetic resonance imaging can be used to acquire images of the whole body, showing these compartments and their distribution. In this article, an automated segmentation algorithm is presented, being able to create tissue profiles of the whole body for tissue classes *subcutaneous AT*, *visceral AT* and *total tissue*. The images are segmented using a fuzzy c-means algorithm, which considers partial volume effects. A separation of the body into anatomic regions along the body axis is done to define regions with visceral AT present. In abdominal image slices, the AT compartments are divided into subcutaneous and visceral compartments using an active contour algorithm. The slice-wise areas of different tissues are plotted against the slice position to obtain their topography. The automatically obtained tissue profiles were compared to profiles created manually by an expert and show high correlation coefficients, indicating similar topography. Absolute error values were calculated for evaluation of the algorithm's absolute accuracy. These show low overall mean values for the classes of total tissue (4.48 %) and visceral AT (3.26 %). The deviation of total AT (sum of visceral and subcutaneous AT) was higher though (8.71 %). Whole examination and analysis time is reduced to less than half an hour.**

***Index Terms*—active contours, adipose tissue profiling, fuzzy c-means, image segmentation, MRI**

I. Introduction

Obesity and overweight are the emerging health problems of the last decades, not only in the western world, but on a worldwide scale [1]. However, not only the amount of total adipose tissue (TAT), but also its distribution and composition is of special importance in the pathogenesis of the concomitant diseases such as metabolic syndrome, type II diabetes or coronary heart disease [2], [3]. Especially the two chemically almost identical, but morphologically and functionally different types of subcutaneous adipose tissue (SCAT) and visceral adipose tissue (VAT) have been reported to be of special interest [4].

MRI enables a reliable quantification of whole body AT as well as the distinction of different compartments [5]. A standardized whole body AT assessment procedure, which is able to show the distribution of all relevant AT compartments as well as the amount of total tissue (TT) in the body, has been proposed [6]. However, the manual segmentation of the images, acquired with this procedure, is time consuming and requires the attention of an expert. Thus, it is desirable to automate this task. Methods for automatic quantification of abdominal AT distributions, distinguishing SCAT and VAT, have been described [7]–[9]. However, none of these approaches is suited for evaluation of image slices of the whole body. A novel procedure, dividing the body into anatomic regions and creating the desired tissue profiles, is proposed in this paper.

II. Materials and Methods

A. MR Data Acquisition

Images were acquired on a clinical 1.5 T whole body scanner (Magnetom Sonata, Siemens Healthcare). During examination, the volunteers were in prone position with extended arms (see Fig. 1). A T1-weighted fast spin echo technique with an echo train length of 7 was applied, using $T_{\mathrm{E}} = 12$ ms, $T_{\mathrm{R}} = 490$ ms, slice thickness 10 mm, 5 slices per sequence and 10 mm gap between slices. Field of view was 450 mm to 530 mm, depending on the volunteer's extension. Images with a 256×178 matrix were recorded, resulting in voxel dimensions of approximately 2 mm $\times$ 2 mm $\times$ 10 mm. Measuring time per sequence was 12 s, allowing breathhold examinations in abdominal and thorax regions. Data was collected from fingers to toes using the scanner's receive/transmit body coil. The given slice thickness and slice spacing resulted in 100 to 130 axial image slices per subject, depending on the volunteer's height. Total examination time was 20 min to 25 min.

B. Fuzzy Clustering

Typical gray value histograms of T1-weighted MR images show three maxima. These correspond to the three prevailing classes background (BG) at the lower end of signal intensity, lean tissue (LT), having intermediate intensities and AT, having high intensity values (see Fig. 2). The notches in between these maxima are not empty, but populated with image elements with an intermediate intensity. These intensities are on the one hand caused by intensity non-uniformities (due to spatial coil characteristics and inhomogeneities of B_0 and B_1) and on

Manuscript received May 11, 2009.

C. Wuerslin is with the Chair of System Theory and Signal Processing, University of Stuttgart, Pfaffenwaldring 47, 70550 Stuttgart, Germany and the Section on Experimental Radiology, University Hospital Tuebingen, Hoppe-Seyler-Str. 3, 72076 Tuebingen, Germany (telephone: +49 711-685-67332, e-mail: christian.wuerslin@lss.uni-stuttgart.de).

B. Yang is with the Chair of System Theory and Signal Processing, University of Stuttgart, Pfaffenwaldring 47, 70550 Stuttgart, Germany (telephone: +49 711-685-67332, e-mail: bin.yang@lss.uni-stuttgart.de).

J. Machann is with the Section on Experimental Radiology, University Hospital Tuebingen, Hoppe-Seyler-Str. 3, 72076 Tuebingen, Germany (telephone: +49 7071-29-80495, e-mail: juergen.machann@med.uni-tuebingen.de).

F. Schick is with the Section on Experimental Radiology, University Hospital Tuebingen, Hoppe-Seyler-Str. 3, 72076 Tuebingen, Germany (telephone: +49 7071-29-80495, e-mail: fritz.schick@med.uni-tuebingen.de).

9781-4244-3962-1/09/$25.00 ©2009 IEEE

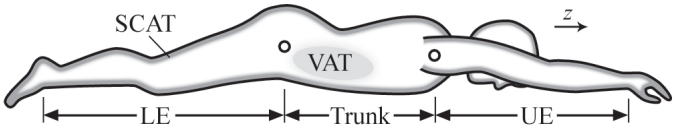

Fig. 1. Volunteer position during examination and distribution of SAT and VAT

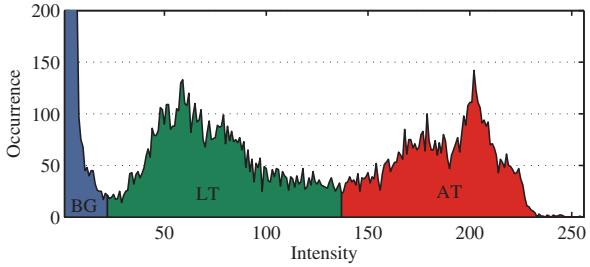

Fig. 2. Typical histogram of a T1-weighted MR image and proposed division into three classes.

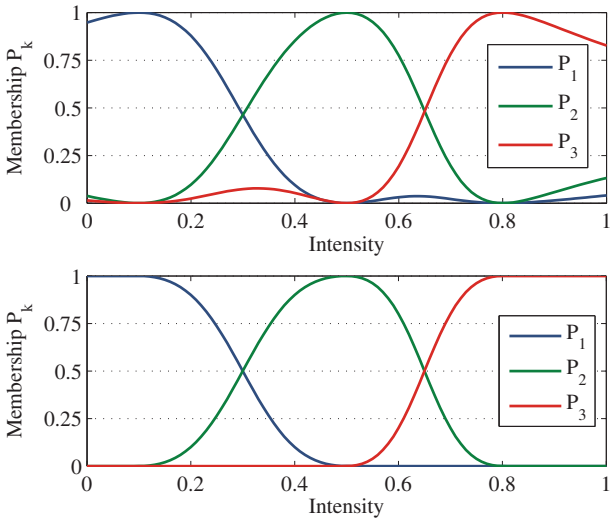

Fig. 3. Class membership probability depending on pixel intensity before (upper) and after correction (lower).

the other hand by partial volume effects. The latter effect is particularly strong, the coarser the spatial resolution of the MR images gets, the first one was reduced by using a spin echo sequence, reducing B_0 inhomogeneities to a great extend.

The first step in segmenting the acquired images into the desired compartments is to distinguish between these three classes by dividing the image histogram into three regions (see Fig. 2). It has been shown, that the so-called fuzzy c-means (FCM) algorithm obtains good results when segmenting MR images according to brightness [10], [11]. Considering an image function $I(\vec{x})$, assigning a scalar gray value (brightness) to each image coordinate $\vec{x} \in \mathcal{I}$, the cost function of the FCM algorithm is given by

$$J_{\mathrm{FCM}} = \sum_{\vec{x}\in\mathcal{I}} \sum_{k=1}^{C} P_k^m\left(\vec{x}\right) \cdot \left(I\left(\vec{x}\right) - v_k\right)^2 . \qquad (1)$$

Here, C is the number of clusters to be used, $P_k(\vec{x})$ is the probability of the pixel at position $\vec{x}$ to belong to cluster k ($k \in [1 \ldots C]$), v_k is the centroid of class k and m is the so-called fuzziness and controls the blending of the membership probabilities. In this implementation we chose $C = 3$ (the three intensity classes mentioned above) and $m = 2$. The cost function J_{FCM} is roughly a measure for the amount of image elements, which are still assigned to the wrong class. Thus, it is desired to minimize J_{FCM} which is archived iteratively by recomputing the cluster centroids v_k and membership probabilities P_k alternately, using (2) and (3):

$$P_k\left(\vec{x}\right) = \frac{\left|I\left(\vec{x}\right) - v_k\right|^{-2/(m-1)}}{\sum_{k=1}^{C}\left|I\left(\vec{x}\right) - v_k\right|^{-2/(m-1)}} \qquad (2)$$

$$v_k = \frac{\sum_{\vec{x}\in\mathcal{I}} P_k^m\left(\vec{x}\right) \cdot I\left(\vec{x}\right)}{\sum_{\vec{x}\in\mathcal{I}} P_k^m\left(\vec{x}\right)} \qquad (3)$$

Though this fuzzy approach is widely used in the segmentation of MR images, the final results of P_k are usually used to create binary (hard) membership masks, by assigning each image element completely to the class k with the highest membership value P_k (maximum membership hard clustering). Though these hard masks will also be needed in some subsequent steps of the proposed algorithm (and will be denoted by M_1, M_2 and M_3) the given application uses the fuzzy membership values as a direct approximation for the partial contribution of different tissues to one image element. This was done because of the relatively coarse resolution of the axial image slices and especially the slice thickness of 10 mm which contributes to a high amount of partial volume effects. However, these fuzzy membership values need to be corrected with respect to a phenomenon, causing irrational results in the given application, as described in the following.

Assuming, a FCM algorithm with $C = 3$ converges, yielding cluster centroids $v_1 = 0.1$, $v_2 = 0.5$ and $v_3 = 0.8$ (brightness values normalized to fundamental range $[0 \ldots 1]$), then the upper plot in Fig. 3 plots the three membership probability functions P_1, P_2 and P_3 versus intensity. Due to the normalization term in the denominator of (2), the membership probabilities sum up to 1 for all intensity values. However, this causes e.g. the membership probability P_3 (AT class) of a very bright pixel ($I(\vec{x}) > v_3$) to decrease again. The value of P_3 even decreases more, the higher the intensity $I(\vec{x})$ gets (see right end of the red line in the upper plot in Fig. 3). This behavior is undesired in the given application, which is why all these irrational segments of P_1, P_2 and P_3 are corrected, resulting in the membership probabilities shown in the lower plot in Fig. 3. The result of this modified FCM clustering, applied to an abdominal image slice can be seen in Fig. 4b.

C. Body Division

In order to define the body region in which the detected AT areas have to be separated into SCAT and VAT, it is helpful to first detect the shoulder- and hip- joints to get an impresion of the extension of the trunk. These joints can be detected by parsing the images for the characteristic pattern, created

by the heads of femur and humerus in axial images. In T1-weighted MR images, because of the high percentage of AT in the long bones of adults, they appear as two circular areas of a certain size and distance. Axial radii of caput humeri and caput femori and their distances were manually measured in ten randomly chosen datasets (five female, five male) to receive a valid target area. Mean values and standard deviation of these measures were calculated to $r = 20.8 \pm 2.2$ mm for the radii, $d_{\mathrm{CF}} = 188.7 \pm 8.3$ mm for the distance between the caput femori and $d_{\mathrm{CH}} = 295.8 \pm 15.8$ mm for the distance between the caput humeri.

Because of the assumption made above, the hard AT mask M_3 is parsed for circular areas. The circularity ρ of an object is calculated by considering the distance d of the object's border pixels to its centroid as a random variable and dividing the variable's mean value μ_d by its standard deviation σ_d:

$$\rho = \frac{\mu_d}{\sigma_d} \tag{4}$$

For this application, a circularity threshold of 6.7 was empirically chosen to separate irregular from circular objects. Hip and shoulder slices are supposed to be detected, when two such circular objects are found with values for radii and distances not farther than three times the standard deviation from the mean of the corresponding empirically determined values, given above. In cases where such circular objects are found in two adjacent slices (e.g. a joint has been cut twice) the slice with the greater radii is chosen to get the z-position nearest to the center of the joint. Due to the slice spacing of 10 mm and slice thickness of 10 mm, in a worst case scenario, the hip and shoulder joints will be found 10 mm away from their actual center.

Anatomically, the region containing VAT was defined as the area reaching from the hip to the lower end of the heart. The lower end of this region is already well defined by the hip slice, obtained previously. Due to the large amount of motion artifacts in the heart area, an automatic detection of the lower heart end was omitted. Instead, this upper margin of the VAT area is calculated using an empirically determined index. This index expresses the upper VAT area end as fraction of the distance between the femoral head and the head of the humerus and was determined to 0.66 from a cohort of 22 datasets ($\sigma = 0.04$).

D. Body Mask Creation

The purpose of this step is to separate the background from objects belonging to the body. As there are also signal-free areas inside the body (e.g. lungs), simply using the inverse of the hard background mask M_1 is not sufficient. However, M_1 is used as starting point for the creation of the body mask. M_1 contains all pixels, with brightness close to zero, thus representing signal-free areas. To exclude signal-free areas inside the body from the background mask, all areas, which are not connected to the upper left corner are deleted. The inverse of this operation contains all body objects. However, special care has to be taken in the thorax area, where images are usually corrupted by a considerable amount of motion artifacts, caused by the beating heart. To eliminate these small objects outside of the body, all objects with an area less than 400 pixels (≈ 16 cm^2) are deleted from the body mask. The situation is more complicated, if the misclassified artifacts are connected to the main body object. To get rid of these undesired extensions, a morphologic opening with a circular kernel with a radius of 20 pixels is applied to the body mask.

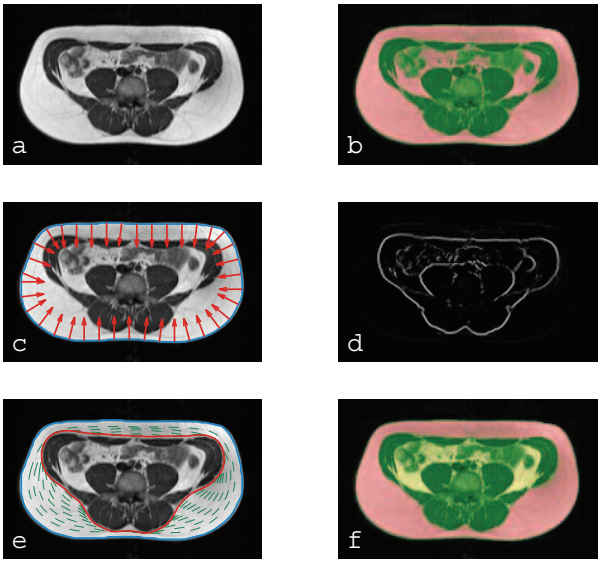

Fig. 4. Visualization of the algorithm steps: **a)** original abdominal image slice, **b)** result of FCM clustering (red: AT, green: LT), **c)** initial alctive contour and deflation forces, **d)** poar edge map used on second active contour step, **e)** active contour evolution, **f)** final result (yellow: VAT, red: SCAT, green: LT)

E. Dividing SCAT and VAT

To obtain the desired tissue profiles, the AT compartments found in the abdominal area have to be divided into the classes SCAT and VAT. Procedures to automatically separate these compartments have been proposed [7]–[9]. The most versatile of these approaches is presented in [7] and uses an active contour algorithm [12] to detect the inner boundary of the SCAT belt. However, active contours usually suffer from two drawbacks: One of them is the reliance on a good initialization contour, the other one is a limited capture range.

To avoid the first problem the proposed algorithm uses the body's outer boundary, extracted from the body mask, as a reliably detectable initialization. The second problem is handled by dividing the active contour's evolution phase into two sub-steps. The first step is designed to pass the bright, gradient-free SCAT belt by using an active contour algorithm with balloon forces [13]. Depending on the application, these additional balloon forces can be used to give the contour a tendency to either in- or deflate (a deflation in this case, see also Fig. 4c). Furthermore, the first step uses relatively large values for the algorithm's membrane weight α (making the contour shrink) and thin-plate weight β (making the contour smooth). The AT probability mask P_3 is used as external energy field E_{ext}. This causes homogeneous areas, such as the SCAT ring to be predominantly force-free. On the inner

TABLE I
THE PARAMETERS USED IN THE TWO-STAGED ACTIVE CONTOUR ALGORITHM

	α	β	γ	k
1^{st} step	0.25	0.5	0.7	0.2
2^{nd} step	0.07	0.05	1	0

edge of the SCAT area, the transition from bright to dark intensity creates force vectors f_x and f_y, pointing opposed to the deflation forces of the balloon contour.

In the second step, an ordinary snake algorithm is used, this time with relatively small values of α and β, enabling the snake to accurately locking on to the edge, separating SCAT and inner tissues. Special care has been taken in choosing an external force for this evolution step. This time, the exact edge positions shall be found. To solve this problem, the image is usually filtered with an edge enhancement filter, such as a Laplacian filter, resulting in high intensity values at image edges and values close to zero in homogeneous areas. In this application, the desired edge is a bright-to-dark transition from the outside to the center of the image. Thus, it is desirable to only lock onto edges in this direction. Thus, a so-called polar edge map is used, containing only such edges, while canceling out transitions in the opposite direction. This radial edge map can be computed by

$$E_{\text{ext}} = -\frac{1}{2}\left(\left|\nabla I\left(\vec{x}\right)\right| + \underbrace{\frac{\vec{x}-\vec{c}}{\left|\vec{x}-\vec{c}\right|}}_{\vec{p}(\vec{x})} \cdot \nabla I\left(\vec{x}\right) \right) , \qquad (5)$$

where $\vec{c}$ is the center pixel of the image and thus $\vec{p}(\vec{x})$ is a vector pointing away from the image center at all positions $\vec{x}$ and normalized in length. Edges, orthogonal to this vector are still considered, but only have half the magnitude of radial bright-to-dark transitions. An example of a polar edge map can be seen in Fig. 4d.

The number of snake points used is determined by a desired minimum inter-point distance of the snake points. Whenever the distance between two adjacent snake points gets below this value (due to snake evolution) one of the points is removed. This value was chosen to one pixel (approximately 2 mm for the given FOV and image resolution), resulting in inter-point distances between 1 and 2 pixels. The values of the snake algorithm (membrane weight α, thin plate weight β, step size γ and weight of the deflation force k) used in the two steps can be found in Table I.

F. Evaluation Procedure

For quantitative analysis of the suggested algorithm, the automatically obtained tissue profiles of 20 volunteers with body mass index (BMI) range 18.5–40.4 (28.4 ± 7.1 kg/m^2) were compared to manually obtained profiles. These manual profiles were obtained using a computer-aided procedure consisting of thresholding the images at two different intensity levels to separate BG, LT and AT. In the abdomen, the amount of VAT was obtained by manually drawing a region of interest. For each dataset and tissue class, two figures were extracted. The first one is the mean over all image slices of the slice-wise absolute tissue difference, expressed as percentage of the amount of manually obtained area of total tissue in that slice:

$$\overline{|\Delta A|} = \frac{1}{N}\sum_{z=1}^{N} \frac{|A_{\text{a}}(z) - A_{\text{m}}(z)|}{A_{\text{TT,m}}(z)} , \qquad (6)$$

where z is the slice index, N the number of image slices in the dataset and $A_{\text{TT,m}}(z)$ is the maually obtained amount of total tissue in the image slice at position z. This value can be considered a measure of the algorithm's accuracy. The second figure is calculated in the same way as the first, except, that it uses simple differences rather than absolute ones. Thus it is calculated by

$$\overline{\Delta A} = \frac{1}{N}\sum_{z=1}^{N} \frac{A_{\text{a}}(z) - A_{\text{m}}(z)}{A_{\text{TT,m}}(z)} . \qquad (7)$$

This value does not represent the algorithms accuracy since positive and negative values might cancel out each other. However, it is a good estimator of whether the algorithm tends to overestimate (positive values) or underestimate (negative values) a certain tissue class.

III. RESULTS

The automatic segmentation algorithm was implemented on a standard mobile computer (Core 2 Duo, 2 GHz, 2 GB RAM) using MATLAB (The MathWorks, Inc). Total segmentation time was 76.1 ± 6.6 s per dataset (105 ± 5.5 image slices per dataset). Structures, limiting the anatomic regions according to section II-C (hips and shoulders) were reliably detected in all volunteers, even if the subject was located slightly tilted in the scanner.

A plot, comparing the automatically and manually obtained tissue profiles of one volunteer is shown in Fig. 5. The dashed lines correspond to the manually obtained profiles, solid lines correspond to the automatically obtained profiles. In Fig. 6, the mean absolute difference values of all tissue classes and all 20 volunteers (calculated using (6)) are shown are plotted against BMI. These values vary in between 2.62 % and 9.41 % for TT, 4.64 % and 14.20 % for TAT (sum of SCAT and VAT in abdominal areas) and 1.18 % and 7.13 % for VAT. In Table II, the average of these values are calculated for four different BMI classes. The mean difference values, indicationg the algorithm's tendency to over- or underestimate certain tissue classes (calculated using (7)), can be found in Table III. These values vary in between -1,12 % and 8.77 % for TT, 3.90 % and 14.20 % for TAT and 1.13 % and 7.13 % for VAT.

IV. DISCUSSION

Due to the increasing world-wide occurrence of obesity and of the resulting complications, such as type II diabetes or coronary complications [1], methods for monitoring AT in the body are of increasing importance. In this, the total amount of AT without considering the location in the body seems to be less promising in the prediction of metabolic complications,

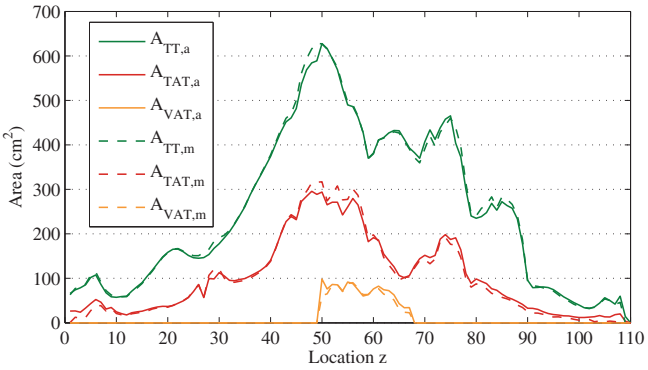

Fig. 5. Comparison of automatically (solid lines) and manually (dashed lines) obtained tissue profiles.

TABLE II
MEAN VALUES OF IN-SLICE ABSOLUTE DIFFERENCES BETWEEN MANUALLY AND AUTOMATICALLY OBTAINED TISSUE AREAS FOR DIFFERENT BMI CLASSES.

BMI Group (kg/m^2)	$\overline{\lvert\Delta A_{\mathrm{TT}}\rvert}$ (%)	$\overline{\lvert\Delta A_{\mathrm{TAT}}\rvert}$ (%)	$\overline{\lvert\Delta A_{\mathrm{VAT}}\rvert}$ (%)
18–24.9	5.63	9.12	4.61
25–29.9	3.90	8.73	2.10
30–34.9	3.16	7.97	2.70
35–40.5	3.91	8.50	3.26
Overall	4.48	8.71	3.26

TABLE III
MEAN VALUES OF IN-SLICE DIFFERENCES BETWEEN MANUALLY AND AUTOMATICALLY OBTAINED TISSUE AREAS FOR DIFFERENT BMI CLASSES.

BMI Group (kg/m^2)	$\overline{\Delta A_{\mathrm{TT}}}$ (%)	$\overline{\Delta A_{\mathrm{TAT}}}$ (%)	$\overline{\Delta A_{\mathrm{VAT}}}$ (%)
18–24.9	3.94	8.71	4.61
25–29.9	1.75	8.34	1.82
30–34.9	0.05	7.13	2.46
35–40.5	0.54	8.13	2.54
Overall	2.07	8.13	3.21

than the precise distinction of specific compartments, such as SCAT and VAT and its spatial distribution [2]–[4]. By using MRI, these compartments can be assessed and used to create standardized tissue profiles of the whole body, while avoiding the use of ionizing radiation [5], [6]. To reduce the time and personal needed for the segmentation of appropriate MR datasets, this paper proposes an integrated method for standardized and region-depended assessment of AT volumes.

The primary goal of the proposed algorithm is to work completely without any user interaction, creating the need of a robust routine. The most challenging step is the division of the body into anatomic regions, which succeeded for all of the volunteers. Also, the separation of SCAT and VAT, using an active contour algorithm achieved the desired results in 98.9 % of all cases, which is also an indicator for the robustness of the method.

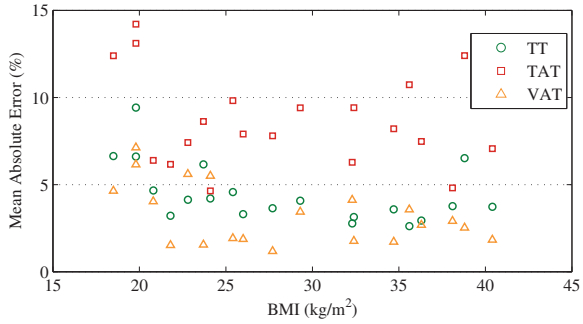

Fig. 6. Mean absolute difference values of all volunteers plotted vs. BMI.

The automatically obtained TT profiles showed good correlation with those, obtained manually (overall mean absolute difference 4.48 %). The TT profiles showed the strongest deviation in the thorax area, where images were heavily corrupted by motion artifacts caused by the heart. The mean absolute differences was significantly above average for the BMI class of normal weight persons where it was 5.63 % and below average for the three remaining classes. The correlation between BMI and mean absolute differences was calculated to $r = -0.49$, indicating a tendency to higher deviation values for lower BMI values. The overall mean difference value of 2.07 % (as given in Table III) shows that the algorithm tends to slightly overestimate the amount of TT. Again, this behavior was stronger for the class of normal weight volunteers, whereas for the two classes of obese volunteers, a tendency was hardly recognizable.

The TAT profiles showed a higher overall mean absolute difference of 8.71 %. Here, the automatically obtained amount of TAT was usually higher in the extremities and significantly higher in feet and hands, as bone marrow was mainly considered as AT by the algorithm. However, the inclusion of bone marrow can easily be compensated for retrospectively, since its amount does not change with BMI. Motion artifacts in the thorax area made an accurate tissue profiling difficult, thus creating high profile deviations. In the class of TAT, the correlation between BMI and mean absolute differences, as well as mean differences was very low. Generally, the mean difference values were very close to those of the mean absolute differences, indicating the algorithm's tendency to overestimate the amount of TAT compared to manual segmentation for all BMI classes.

The VAT profiles showed a lower overall mean absolute difference than TAT (3.28 %). This good correlation is especially desirable, as VAT is the main subject of this method. Just like for TT, this value was above average for the class of normal weight volunteers (4.52 %) and below average for all other classes. The values of the mean differences again show that the algorithm tends to overestimate the amount of VAT in a vast majority of cases (overall 3.21 % overestimation).

A visual inspection of the segmented images showed that the overestimation of VAT in the class of normal weight volunteers (BMI < 25) was mainly caused by the lack of a significant

amount of AT in the abdominal area. This causes the FCM-algorithm to detect the bone marrow of pelvis and spine (which is slightly brighter than surrounding LT, but usually detected as LT in obese volunteers) to be detected as VAT. In very lean subjects (BMI < 20) even parts of the liver were detected as VAT due to the lack of AT present.

In conclusion, this paper proposes a robust, automatic segmentation method, supplying standardized whole-body AT profiles for metabolism risk indication and intervention monitoring. The proposed algorithm is capable to reduce the total examination time to less than 30 minutes.

REFERENCES

[1] WHO, "Obesity: preventing and managing the global epidemic," Tech. Rep. 894, World Health Organization, 2000.

[2] M. Krotkiewski, P. Björntorp, and L. Sjöström, "Impact of obesity on metabolism in men and women. Importance of regional adipose tissue distribution," *J. Clin. Invest.*, vol. 72, pp. 1150–1162, 1983.

[3] B. Larsson, C. Bengtsson, P. Björntorp, L. Lapidus, L. Sjöström, and et al., "Is abdominal body fat distribution a major explanation for the sex difference in the incidence of myocardial infarction? The study of men born in 1913 and the study of women, Göteborg, Sweden.," *Am. J. Epidemiol.*, vol. 135, pp. 266–273, Feb 1992.

[4] B. L. Wajchenberg, "Subcutaneous and visceral adipose tissue: their relation to the matabolic syndrome," *Endocr. Rev.*, vol. 12, pp. 697–738, 2000.

[5] N. Abate, D. Burns, R. M. Peshock, A. Garg, and S. M. Grundy, "Estimation of adipose tissue mass by magnetic resonance imaging: Validation against dissection in human cadavers," *J. Lipid. Res.*, vol. 35, pp. 1490–1496, 1994.

[6] J. Machann, C. Thamer, B. Schnoedt, M. Haap, H.-U. Haring, and et al., "Standardized assessment of whole body adipose tissue topography by MRI," *J. Magn. Reson. Imaging*, vol. 21, pp. 455–462, 2005.

[7] V. Positano, A. Gastaldelli, A. M. Sironi, M. F. Santarelli, M. Lombardi, and et al., "An accurate and robust method for unsupervised assessment of abdominal fat by MRI," *J. Magn. Reson. Imaging*, vol. 20, pp. 684–689, 2004.

[8] T.-H. Liou, W. P. Chan, L.-C. Pan, P.-W. Lin, P. Chou, and et al., "Fully automated large-scale assessment of visceral and subcutaneous adipose tissue by magnetic resonance imaging," *Int. J. Obes. Relat. Metab. Disord.*, vol. 30, pp. 844–852, 2006.

[9] J. Kullberg, H. Ahlström, L. Johannson, and H. Frimmel, "Automated and reproducible segmentation of visceral and subcutaneous adipose tissue from abdiminal MRI," *Int. J. Obes. Relat. Metab. Disord.*, vol. 31, pp. 1806–1817, 2007.

[10] J. C. Bezdek, L. O. Hall, and L. P. Clark, "Review of MR image segmentation techniques using pattern recognition," *Med. Phys.*, vol. 20, pp. 1033–1048, 1993.

[11] L. O. Hall, A. M. Bensaid, L. P. Clarke, R. P. Velthuizen, M. S. Silbiger, and et al., "A comparison of neural network and fuzzy clustering techniques in segmenting magnetic resonance images of the brain," *IEEE Trans. Neural Networks*, vol. 3, pp. 672–682, September 1992.

[12] M. Kass, A. Witkin, and D. Terzopoulos, "Snakes: Active contour models," *Int. J. Comput. Vision*, vol. 1, pp. 321–331, 1988.

[13] L. D. Cohen, "On active contour models and balloons," *CVGIP: Image Underst.*, vol. 53, pp. 211–218, 1991.